RESEARCH ARTICLE

Key Points:
- An empirical magnetosphere model is developed with a realistic IMF B_y-controlled spiral structure of dayside field-aligned currents
- The model includes a new magnetic bubble representation of polar cusp field depressions due to diamagnetism of injected magnetosheath plasma
- Dayside cusp response to external drivers and dipole tilt effects is studied based on hybrid method of fitting the model to spacecraft data

Correspondence to:
N. A. Tsyganenko,
n.tsyganenko@spbu.ru

Empirical Modeling of Dayside Magnetic Structures Associated With Polar Cusps

N. A. Tsyganenko[1] [iD] and **V. A. Andreeva[1]** [iD]

[1]Institute and Department of Physics, Saint-Petersburg State University, Saint-Petersburg, Russia

Abstract The magnetic structure of dayside polar cusps is intimately related to the high-latitude field-aligned currents (FACs) and the cross-**B** diamagnetic currents due to the penetrated plasma of magnetosheath origin. The dayside FAC configuration is sensitive to the azimuthal component of the interplanetary magnetic field, manifested in the latitudinal splitting and longitudinal overlapping of the Region 1 FAC zone around noon. The diamagnetism of the polar cusp plasma results in deep cleft-shaped depressions of the ambient magnetic field. Neither of the above factors have yet been properly addressed in the existing empirical models of the distant magnetosphere. To fill this gap, an advanced data-based model has been developed, including the spiral structure of the dayside FACs and their splitting/overlapping in response to the orientation and magnitude of the azimuthal interplanetary magnetic field component B_y. The cusp diamagnetic field depressions are modeled using a new approach, based on a 3-D system of magnetic "bubbles" (Tsyganenko & Andreeva, 2018, https://doi.org/10.1029/2018GL078714). The magnetic effects associated with FACs and diamagnetic currents are represented within the framework of a single hybrid model, fitted to large subsets of spacecraft data. The obtained results are analyzed in the context of the dayside magnetic field response to interplanetary conditions and the geodipole tilt angle.

Plain Language Summary This work deals with the solar windward side of the Earth's magnetosphere, which is most exposed to the incoming flow of interplanetary plasma, and, as such, takes the first blow during space storms. The Earth's magnetic field interconnects there with the field carried from Sun, which results in a complex system of electric currents flowing along the magnetic field lines down to the ionosphere and then back into the interplanetary space. These currents conduct the solar wind momentum and energy into the magnetosphere and are sensitive to the orientation of the interplanetary magnetic field. Another unique feature of the dayside magnetosphere is a pair of deep funnel-shaped holes on its boundary, called polar cusps, a kind of weak spots where the solar wind plasma is injected into the magnetosphere and suppresses the local magnetic field. In spite of huge amount of data collected since the beginning of the space era, these factors have not yet been properly included in the existing models, and the present paper describes an attempt to fill this gap. Based on large sets of spacecraft data and novel techniques, we developed a new model which incorporates and quantitatively describes both the above features.

1. Introduction

The magnetospheric polar cusps are formed due to a specific topological property of a dipole field confined within a superconducting boundary. An essential element of such a vacuum magnetic configuration is a pair of null points on the magnetopause, where the high-latitude field lines diverge and flare out along the boundary. In the real magnetosphere, the null points evolve into longer and wider cleft-like regions, filled with relatively cold and dense plasma of magnetosheath origin. Due to the diamagnetism of the injected plasma, the vacuum field depressions, initially localized near the boundary, expand in space, protrude inward, and deepen in magnitude, forming extended "funnels" with a weak magnetic field (Farrell & Van Allen, 1990). Fairfield (1991) compared dayside observations of IMP-4,5,6, IMP-D, and HEOS-1,2 satellites with predictions of an empirical model and found broad regions of depressed field at high latitudes, associated with the cusp plasma diamagnetism and unaccounted for by then existing models. Using data of Polar satellite, Tsyganenko and Russell (1999) studied the radial/azimuthal distribution of the cusp depression and its dependence on the geodipole tilt angle and suggested a method to include it in the empirical models, based on a local transverse stretching of the magnetic field.

In a more recent paper based on both Polar and Cluster data (Tsyganenko, 2009), a detailed statistical study was made of the depression magnitude and its spatial distribution as a function of the dipole tilt. A noteworthy finding in that work was a high correlation between the observed B_y inside the cusp funnels and the interplanetary magnetic field (IMF) B_y. It was also shown that the corresponding linear regression coefficient monotonically and dramatically (fivefold) increased with decreasing geocentric distance from 2.4 at $R \sim 6.5$ to 12.6 at $R \sim 2.5$. Such an impressive steepness and regularity was demonstrated to quantitatively agree with the interpretation of the observed IMF "penetration" into the cusps as a combined result of a shear-like duskward/dawnward shift of the downward/upward (prenoon/postnoon) parts of the region 1 field-aligned current (R1 FAC) system, accompanied by a latitudinal separation between their overlapping prenoon and postnoon segments. The spatial extent, magnitude, and direction of the shifts, controlled by the magnitude and sign of IMF B_y, were discussed in many earlier publications (e.g., Erlandson et al., 1988; McDiarmid et al., 1979; Reiff & Burch, 1985), as well as in more recent works (Carter et al., 2016; Korth et al., 2010, 2011; Laundal et al., 2018; Tenfjord et al., 2015, and references therein). While the cusp depression is a relatively local effect and, as such, does not dramatically affect the global field line mapping, the transverse zonal field due to the IMF-related deformation of R1 FACs may result in significant azimuthal shifts of the field line footpoints, an interesting subject for future studies.

Neither the diamagnetic depression nor the IMF B_y effects in the dayside FACs have been properly taken into account in existing empirical models of the distant magnetospheric field, and the goal of this work is to fill that gap. In the present paper we describe and discuss new methods to represent the cusp electric current systems and the associated magnetic fields. Based on the developed techniques, a pilot version of the new model is constructed and fitted to subsets of space magnetometer data taken in the inner and distant magnetosphere, binned into intervals of the B_z component of IMF.

The article is organized as follows. Section 2 describes the basic structure of the model, including the principles of constructing the R1 FAC and cusp depression components. Section 3 overviews the database used in this study. Section 4 presents main results of fitting the model to the data. Section 5 discusses the obtained results and summarizes the work.

2. Basic Structure of the Model: Background Field and the Cusp-Related Modules

In this study, we follow the approach developed in earlier data-based models, reviewed in Tsyganenko (1990, 2013). Its essence is to represent the total magnetic field as a sum of partial fields associated with principal current systems, namely, the magnetopause, the tail current (TC), the ring current (RC; composed in turn of its symmetric and partial components [SRC and PRC, respectively]), the R1 FACs, and, finally, the newly added cusp diamagnetic (CD) current system. We also note from the outset that the Region 2 FAC system is viewed as an integral component of the PRC and, as such, is not singled out as a separate source.

Since this study is focused on the relatively local dayside cusp region, the natural first step is to build a first-order "background" approximation for the magnetospheric field, composed of contributions from the magnetopause, TC, SRC, PRC, and the original R1 FAC module, in which the IMF B_y effects are temporarily turned off. Once the initial set of parameters is derived from the data, the next steps are to unfix the IMF B_y-related parameters in the R1 FAC module, then include the diamagnetic CD source and, finally, refine the model in the last fitting round. Such a successive correction procedure is at the core of the "hybrid" approach, introduced in our recent work (Tsyganenko & Andreeva, 2017).

To generate the first-approximation field, we employed the modules of a recent *TA15* model (Tsyganenko & Andreeva, 2015); the reader is referred to that paper for a detailed description of its structure. In the present work, the original R1 FAC module of *TA15* underwent significant modifications made in order to reproduce the IMF B_y effects. The next section presents a more detailed account of both the original R1 FAC model and of the novel features introduced in its modified version.

2.1. Modeling the Field of Region 1 FACs

The R1 FAC model represents the corresponding magnetic field as a sum of contributions from a set of partially overlapping spread-out current flow tubes, which form a 3-D funnel-shaped flared layer crossing the ionosphere along the expected location of the R1 FAC oval. At low altitudes, the dawnside (downward) and duskside (upward) currents flow along nearly dipole-like field lines, while at larger distances, they gradually depart toward higher latitudes. Although the geometry of the model R1 FAC system was already
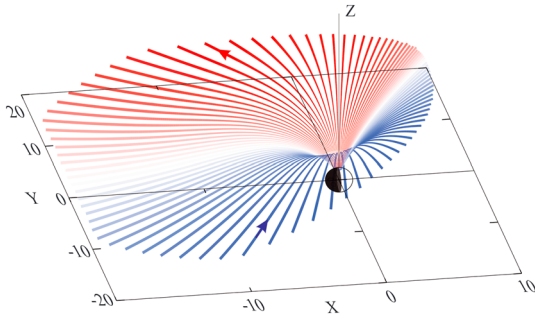
Figure 1. Large-scale configuration of the Region 1 field-aligned current flow lines in the base *TA15* model. Blue/red lines in the morning/evening sectors correspond to downward/upward currents. Only the northern half of the entire system is shown. At large distances, the currents close via the magnetopause, while at low altitudes, they connect via the Earth's center (see text).

described and illustrated in detail in several previous works (e.g., Figures 3 and 4 of Tsyganenko, 2013; Figure 7 of Tsyganenko, 2014; Figure 10 of *TA15*), we nevertheless chose to reproduce it again in Figure 1, in order to keep the paper more consistent and self-contained.

Note that Figure 1 shows only the intramagnetospheric part of the total R1 FAC system. As detailed in the earlier publications, the currents close via the model magnetopause in such a way that the total field is kept inside the magnetosphere. At low altitudes, the downward and upward currents connect via the Earth's center, rather than over the ionosphere. As demonstrated in Tsyganenko, (2002, section 2.3.4), such an assumption affects only the low-altitude magnetic field but has virtually no effect in more distant areas above $R \sim 2 R_E$ and, hence, does not result in any tangible modification of the magnetic field line mapping.

In the next section we concentrate mostly on the new elements of the model and, to that end, start from basic equations describing the R1 FAC system configuration and calculation of its contribution to the total magnetic field.

2.1.1. Geometry of the Model R1 FAC System

In the case of untilted Earth's dipole, the global funnel-like FAC surface shown in Figure 1 is defined in the solar-magnetic (SM) spherical coordinates $\{r, \theta, \phi\}$ by a compact equation

$$\theta(r, \phi) = \arcsin \left\{ \frac{r}{\left\{ r^\alpha + [\sin \theta_i(\phi)]^{-2\alpha} - 1 \right\}^{1/\alpha}} \right\}^{1/2}, \tag{1}$$

first proposed in a somewhat different form by Tsyganenko and Stern (1996, equations 2 and 3) and then repeatedly used in more recent models; see a review of Tsyganenko (2013) and references therein. The parameter α controls the distant configuration of the surface (1), such that larger values of α correspond to a more dipole-like shape at middle latitudes. At even lower latitudes, the surface gradually departs outward from the quasi-dipolar shells and asymptotically stretches parallel to the equatorial plane in the limit $r \to \infty$.

The function $\theta_i(\phi)$ in the denominator of (1) is the longitudinally varying colatitude of the funnel intersection with the ionosphere, defining the low-altitude shape of the R1 FAC oval. In the above referenced earlier models, the colatitude $\theta_i = \theta_i(\phi)$ was represented by a single equation $\theta_i = \theta_0 + \Delta\theta_0 \sin^2(\phi/2)$, which resulted in a closed dawn-dusk symmetric R1 FAC oval, crossing the noon and midnight meridians at colatitudes θ_0 and $\theta_0 + \Delta\theta_0$, respectively. In the present model, by contrast, the duskside and dawnside parts of the R1 FAC oval are represented separately, with the corresponding ionospheric colatitudes being assumed for the northern hemisphere (hence the superscript N) in the form

$$\theta_{i,\text{dusk}}^{(N)}(\phi) = \theta_0 + \Delta\theta_0 \sin^2 \frac{\phi'(\phi)}{2} - \Delta\theta_1 \cos^2 \frac{\phi'(\phi)}{2} - \gamma \Psi \cos[\phi'(\phi)], \tag{2}$$

$$\theta_{i,\text{dawn}}^{(N)}(\phi) = \theta_0 + \Delta\theta_0 \sin^2 \frac{\phi'(\phi)}{2} + \Delta\theta_1 \cos^2 \frac{\phi'(\phi)}{2} - \gamma \Psi \cos[\phi'(\phi)] . \tag{3}$$

The function $\phi'(\phi)$ in the right-hand side of (2) and (3) is defined as

$$\phi'(\phi) = \pi \frac{\phi + \Delta\phi}{\pi + \Delta\phi}, \tag{4}$$

such that the azimuthal angle ϕ' in the right-hand side of (2) and (3) spans the intervals $[0, \pi]$ and $[\pi, 2\pi]$, as the SM longitude ϕ varies within the intervals $[-\Delta\phi, \pi]$ and $[\pi, 2\pi + \Delta\phi]$, respectively. The angle $\Delta\phi$ quantifies the extent of the overlap of the upward (duskside) portion of FACs across the noon meridian into the dawn sector and of the downward (dawnside) FACs into the dusk sector. The parameter $\Delta\theta_1$ defines the latitudinal split between the dawnside and duskside branches of the R1 FAC zone around noon. Specifically, by construction of equations (2)–(4), both the colatitudes $\theta_{i,\text{dusk}}$ and $\theta_{i,\text{dawn}}$ assume the same value $\theta_0 + \Delta\theta_0$ at $\phi = \pi$ (which ensures the oval's continuity at midnight) but diverge from each other around noon so that $\theta_{i,\text{dusk}} = \theta_0 - \Delta\theta_1$ and $\theta_{i,\text{dawn}} = \theta_0 + \Delta\theta_1$.
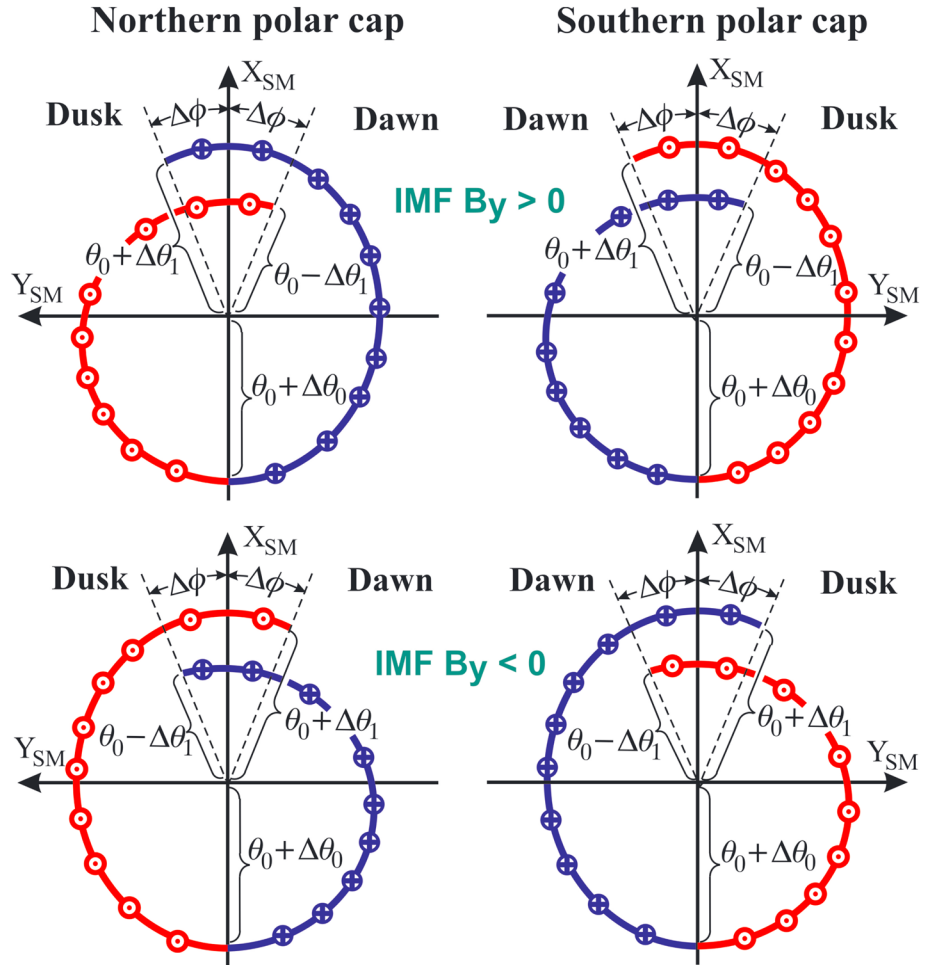
Figure 2. Illustrating low-altitude geometry of the model region 1 field-aligned current zones, as viewed from above the Northern (left) and Southern (right) polar caps, with the dayside split/overlap polarity and extent controlled by the IMF B_y. Blue and red segments correspond to the downward and upward currents at dawn and dusk, respectively. Top and bottom rows correspond, respectively, to positive and negative polarities of IMF B_y, inducing positive and negative B_y inside the cusps. IMF = interplanetary magnetic field; SM = solar-magnetic.

The last term in the right-hand sides of (2) and (3) represents the seasonal/diurnal latitude shift, or "slippage," of the FAC ionospheric footpoints with varying geodipole tilt Ψ. The slippage is assumed as a linear function of the tilt angle, with the proportionality coefficient γ. The $\cos[\phi'(\phi)]$ factor implies a nearly uniform sunward/antisunward displacement of the entire FAC zone as a whole in response to the dipole tilt. This effect was detected using dayside particle precipitation data still in late 1980s (Newell & Meng, 1989) and was confirmed by model calculations of the tilt-related shift of the polar cusps (Tsyganenko, 1990, see Figure 52 there). In those studies, the shift was found to be a nearly linear function of the tilt angle, varying within $\pm 2°$ in the entire range $-30° \leq \Psi \leq +30°$ of the dipole tilt.

In analogy to equations (2) and (3) for the northern hemisphere, a similar pair of equations is introduced to describe the configuration of the southern FAC zone:

$$\theta_{i,\text{dusk}}^{(S)}(\phi) = \pi - \theta_0 - \Delta\theta_0 \sin^2 \frac{\phi'(\phi)}{2} - \Delta\theta_1 \cos^2 \frac{\phi'(\phi)}{2} - \gamma\,\Psi \cos[\phi'(\phi)], \qquad (5)$$

$$\theta_{i,\text{dawn}}^{(S)}(\phi) = \pi - \theta_0 - \Delta\theta_0 \sin^2 \frac{\phi'(\phi)}{2} + \Delta\theta_1 \cos^2 \frac{\phi'(\phi)}{2} - \gamma\,\Psi \cos[\phi'(\phi)] . \qquad (6)$$

Here we assume that, in the untilted case $\Psi = 0$, the dawnside/duskside part of the southern R1 FAC zone is mirror symmetric to the duskside/dawnside segment of the northern zone with respect to the SM equatorial plane. Accordingly, the colatitude parameter θ_0 is replaced here with $\pi - \theta_0$, while the noon-midnight shift

$\Delta\theta_0$ and the near-noon splitting parameter $\Delta\theta_1$ have opposite signs to those in the northern hemisphere. The tilt-dependent slippage terms, however, remain unchanged due to the fact that, for any $\Psi \neq 0$, both northern and southern cusps shift in the same direction. Based on the above cited observation/modeling results, we further assume that their latitudinal shifts are linear and, hence, north-south antisymmetric with respect to Ψ.

The above analytical description of the dayside FAC geometry at the ionospheric altitude is illustrated in Figure 2. Two panels in each row show the shapes of the northern (left) and southern (right) FAC zones for positive (top) and negative (bottom) polarities of IMF B_y.

Whereas at the ionospheric level the tilt effects reduce to a relatively small slippage of the cusp and R1 FAC footpoints, they become much more pronounced in the distant magnetosphere, where the quasi-dipolar inner field gradually transforms into the antisunward-oriented tail-like configuration. This prompts to apply a suitable radially growing deformation of coordinates or *spacewarping*.

In this model, we adopt a deformation similar to that used in *TA15*, in which any point of space with SM coordinates $\{r, \theta, \phi\}$ and $\rho = r \sin \theta$ is rotated to a new location $\{r, \theta', \phi\}$ with

$$\theta'(r, \phi) = \theta(r, \phi) + \frac{H}{r} \sin \theta(r, \phi), \tag{7}$$

$$\text{where} \quad H = R_H \tan \Psi \left\{ \left[1 + \left(\frac{\rho}{R_H} \right)^\beta \right]^{1/\beta} \right\}. \tag{8}$$

Here the fixed parameter $R_H = 8 R_E$ is physically equivalent to the hinging distance in the *TA15* tail module and, for that reason, was set numerically close to its standard value. It defines the radial distance to the transition boundary, where the dipole-dominated inner magnetosphere gradually transforms into the outer solar-wind-controlled windsock domain, with the parameter $\beta = 4$ quantifying the smoothness of the change.

Finally, while in all previous models, the α parameter in (1) was set at a single constant value; in the present treatment, we adopt a more flexible form, such that α is allowed to smoothly vary between $\alpha = \alpha_n$ at noon and $\alpha = \alpha_m$ at midnight:

$$\alpha(\phi) = \alpha_n + (\alpha_m - \alpha_n) \sin^2(\phi/2). \tag{9}$$

The rationale behind this modification is to more flexibly decouple from each other the dayside and nightside parts of the R1 FAC layer: the dayside FACs not only map to higher latitudes in the ionosphere but may also be significantly deflected toward the terminator in the distant polar magnetosphere. On the nightside, by contrast, the R1 currents map to lower latitudes and are expected to merge with the plasma sheet boundary layer in the tail (e.g., Kaufmann et al., 2003; Tsyganenko & Stern, 1996; Tsyganenko et al., 1993).

2.1.2. Calculation of the R1 FAC Magnetic Effects

Derivation of the R1 FAC magnetic field via the piecewise Biot-Savart summation was earlier addressed in a review (Tsyganenko, 2013, Section 3.2); to make the paper more self-contained, we briefly recapitulate here the main points. The starting point is to represent the contribution at a location $\mathbf{r}$ from each individual FAC flow line with the current I via the vector potential

$$\mathbf{A}(\mathbf{r}) = \frac{\mu_0 I}{4\pi} \oint \frac{d\mathbf{r}'}{|\mathbf{r} - \mathbf{r}'|}, \tag{10}$$

where the integration is done over the entire circuit, including the ionospheric closure current, the magnetospheric FAC segments, and the most distant current in the magnetosheath. As detailed elsewhere (Sotirelis et al., 1994), the contribution from the extramagnetospheric part of the current system is effectively taken into account by adding an appropriate shielding field. The magnetic effect of ionospheric closure currents is important only at low altitudes within $r \leq 2 R_E$ (see a quantitative discussion in Tsyganenko, 2002, Section 2.3.4 and Figure 6). In the present case, the modeling domain is bounded from below by $r \sim 2 - 3 R_E$, which allows us to ignore the actual pattern of the ionospheric closure currents and instead close the FACs through the Earth's center. (Note that, following the Fukushima's theorem, such a simplification is equivalent to closing the FACs through a uniformly conducting ionosphere.)

The next assumption, made in order to avoid singularity in (10) at $\mathbf{r} = \mathbf{r}'$, is to replace $|\mathbf{r} - \mathbf{r}'|$ with $\sqrt{|\mathbf{r} - \mathbf{r}'|^2 + D^2}$. The regularization parameter D varies along the current flow tube as $D = D_0 r^\zeta$, which
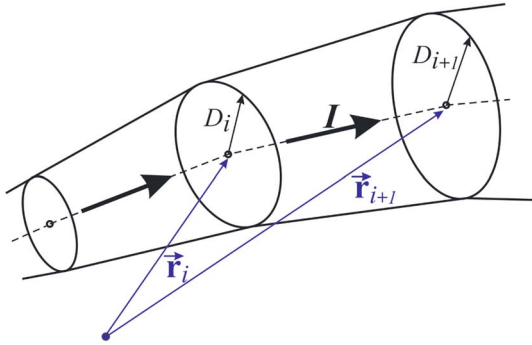
Figure 3. Illustrating the calculation of the field-aligned current net magnetic effect by summation over a set of finite current segments. In actuality, the current is diffusely spread out across the tube without sharp boundaries (shown here only for illustrative purposes, with D_i being the scale radii of the current density falloff).

allows the FACs to diverge or converge in concert with the magnetic field lines and thus keeps them nearly field-aligned. The entire FAC flow tube is represented as a chain of adjacent segments of finite length, as sketched in Figure 3. Assuming a locally linear variation of the D^2 term between the ends of the segment, the vector potential is reduced to a closed analytical form, first published in our earlier work on the substorm current wedge modeling (Sergeev et al., 2011):

$$\mathbf{A} = \frac{\mu_0 I}{4\pi} \sum_i \frac{\mathbf{r}'_{i+1} - \mathbf{r}'_i}{\sqrt{E_i}} \ln \frac{2E_i + F_i + 2\sqrt{E_i(E_i + F_i + G_i)}}{F_i + 2\sqrt{E_i G_i}}, \tag{11}$$

where

$$E_i = (\mathbf{r}'_{i+1} - \mathbf{r}'_i)^2 + (D_{i+1} - D_i)^2, \tag{12}$$

$$F_i = 2(\mathbf{r} - \mathbf{r}'_i) \cdot (\mathbf{r}'_i - \mathbf{r}'_{i+1}) + 2D_i(D_{i+1} - D_i), \tag{13}$$

$$G_i = (\mathbf{r} - \mathbf{r}'_i)^2 + D_i^2, \tag{14}$$

from which analytical expressions for the magnetic field components are readily obtained in a straightforward manner by differentiation.

As noted above, the global R1 FAC system was constructed by combining the individual spread-out wires into a set of partially overlapping current filaments of finite transverse thickness. The total number of the current wires was set equal to 40 in both dawnside (downward) and duskside (upward) parts of the FAC layer, which ensured a smooth azimuthal distribution of the current density. The corresponding parameters D_0 and ζ were fixed from the outset at the values 320 km (i.e., on the order of 3° of latitude at $r = 1\,R_E$) and 1.3, respectively, for all local times. No attempt was made here to derive the parameter D_0 from data; as found in many earlier experiments, the lack of observations below $r \leq 3 - 4\,R_E$, as well as the dynamical nature of the FAC geometry does not allow to properly resolve their low-altitude thickness from the distant data. As for the flaring exponent ζ, the value 1.3 was assumed slightly lower than the theoretical estimate 1.5, corresponding to the outward expansion rate of a purely dipolar field line tube (e.g., Tsyganenko, 2009, Section 5).

The current strength in the wires was assumed to vary with longitude as $\sin \phi'(\phi)$, where the angle ϕ' is defined by (4). This implies that, for IMF $B_y \neq 0$, the FAC density peaks at $\phi_{\text{dusk}} = (\pi - \Delta\phi)/2$ and at $\phi_{\text{dawn}} = (3\pi + \Delta\phi)/2$, that is, in the early dusk and late dawn sectors, respectively, while in the case of IMF $B_y = 0$, their distribution becomes strictly symmetric with respect to the dawn-dusk meridian plane. In such a formulation, the total downward current is always kept equal to the total upward current. Note that the model can be further generalized by adding higher-order Fourier components of the FAC density, varying as $j \sim \sin[m\phi'(\phi)]$ where $m = 2, 3, \ldots$. Such a modification would enable the model to reproduce the FAC localization near the noon meridian, observed during northward IMF periods. Another research area, definitely worth of attention in future studies, is the FAC closure in the magnetosphere. In the present model the current flow lines, by construction, lie in the SM meridional planes, while their actual closure paths can deflect in the azimuthal direction, either toward the magnetopause or across the midnight meridian plane. Inclusion of the azimuthal component in the FAC system will increase the model's flexibility and, potentially, provide interesting further insights.

To complete this section, we briefly overview the variable and fixed parameters of the new FAC model. Following the *TA15* approach, the R1 FAC parameters were grouped into linear coefficients and nonlinear parameters, of which the first ones defined the overall total current in the system and its dipole tilt dependence, while the nonlinear group described the geometry of the FAC layer. Specifically, the variable nonlinear parameters were (i) the noon colatitude θ_0 and its noon-midnight increment $\Delta\theta_0$ in (2)–(6), (ii) the proportionality coefficients relating the noon FAC splitting angle $\Delta\theta_1$ and the longitudinal overlap $\Delta\phi$ with the IMF B_y (see equation (26) below), (iii) the R1 FAC surface parameters α_n and α_m entering in (9), and, finally, (iv) the tilt-related slippage parameter γ entering in (2)–(6).

2.2. Modeling the Cusp Diamagnetism Effects Using the Bubble Basis Functions

In an early publication (Tsyganenko & Russell, 1999), the CD depressions were modeled using a local transverse deformation of the near-noon high-latitude magnetic field. Although mathematically convenient and computationally fast, that method does not conserve $\nabla \times \mathbf{B}$; as a result, the model currents may be sensitive to small details of the deformation function, making it difficult to avoid unphysical side effects. In the present

work, we employed instead a hybrid method (Tsyganenko & Andreeva, 2017), in which the diamagnetic part of the cusp field enters in the total field via a separate set of higher-order correction terms, represented by multiple diffuse "bubble" sources (Tsyganenko & Andreeva, 2018).

The bubble representation is somewhat similar to the earlier developed radial basis function method (Tsyganenko & Andreeva, 2016). In our specific case, its implementation is facilitated by the fact that the cusp depressions are relatively confined in space and the magnetic disturbance vector associated with the diamagnetism is nearly field-aligned, whereas the FAC-related magnetic fields are mostly transverse. This prompts to derive the model parameters in two steps. At the first step, the diamagnetic sources are ignored, and the modular part of the model is fitted to data. The output is a set of residual magnetic field vectors, each of which being equal to the difference between the observed field vector and that provided by the modular part of the model. The obtained set of residual field vectors is then used as input for the derivation of the bubble expansion coefficients in the second fitting round.

The main principles of the bubble model construction were recently described in Tsyganenko and Andreeva (2018), to which paper the reader is referred for additional details. To reiterate the most essential points, the model field is a linear combination of contributions from a set of spatially distributed axisymmetric electric current vortices, placed at the nodes $\{x_i, y_i, z_i\}$ of a 3-D grid. Each node bears two mutually orthogonal sources, oriented in the X_{SM} and Z_{SM} directions, and each source is described in its own local node-centered cylindrical coordinate system $\{\rho, \phi, z\}$ by the vector potential

$$\Delta \mathbf{a} = \frac{\rho \mathbf{e}_\phi}{\left[1 + (\rho^2 + z^2)/R_0^2\right]^\varepsilon} \, . \tag{15}$$

The magnetic field components corresponding to the X- and Z-oriented sources (denoted below by the superscripts $\{X\}$ and $\{Z\}$) read, respectively,

$$b_{x,i}^{\{X\}} = F(r')\left[r'^2 + R_0^2 - \varepsilon(y'^2 + z'^2)\right], \qquad b_{y,i}^{\{X\}} = F(r')\varepsilon\, x'y', \qquad b_{z,i}^{\{X\}} = F(r')\varepsilon\, x'z', \tag{16}$$

$$b_{x,i}^{\{Z\}} = F(r')\varepsilon\, x'z', \qquad b_{y,i}^{\{Z\}} = F(r')\varepsilon\, y'z', \qquad b_{z,i}^{\{Z\}} = F(r')\left[r'^2 + R_0^2 - \varepsilon(x'^2 + y'^2)\right], \tag{17}$$

where $x' = x - x_i$, $y' = y - y_i$, $z' = z - z_i$, $F(r') = (r'^2 + R_0^2)^{-(\varepsilon+1)}$ and $r'^2 = x'^2 + y'^2 + z'^2$. The parameters R_0 and ε define the bubble radial extent and the asymptotic field behavior; in particular, $\varepsilon = 3/2$ corresponds to dipole-like sources with a vacuum field at $r' \gg R_0$. The magnitude factors are intentionally omitted in (16) and (17), since the vectors $\mathbf{b}_i^{\{X\}}$ and $\mathbf{b}_i^{\{Z\}}$ will enter in the model field as basis functions with a priori unknown coefficients.

In the above cited work, the bubble model was used to reconstruct "instantaneous" magnetic field configurations obtained from MHD simulation runs for a single value of the Earth's dipole tilt angle, which allowed us to avoid making any assumptions about the tilt-related deformation of the model field. In the present study, by contrast, we deal with real data taken at different times with different geodipole tilt angles, which makes it necessary to set symmetry constraints, needed to analytically parameterize the model with the tilt angle Ψ. A natural way of doing this is to represent the generally asymmetric model field $\mathbf{B}(x, y, z, \Psi)$ with a linear combination of partial fields $\mathbf{B}^\perp(x, y, z)$ and $\mathbf{B}^\|(x, y, z)$, whose symmetry properties correspond, respectively, to the perpendicular ($\Psi = 0$) and parallel ($\Psi = 0$) dipole orientations:

$$\mathbf{B}(x, y, z, \Psi) = \mathbf{B}^\perp(x, y, z)\cos\Psi + \mathbf{B}^\|(x, y, z)\sin\Psi \, . \tag{18}$$

The components $\{B_x^\perp, B_y^\perp, B_z^\|\}$ and $\{B_x^\|, B_y^\|, B_z^\perp\}$ must be odd and even functions of z, respectively, in order that the total field components meet the basic symmetry relations (e.g., Mead & Fairfield, 1975, Equations (4)–(6); Andreeva & Tsyganenko, 2016, Equation (4)):

$$B_{x,y}(x, y, z, -\psi) = -B_{x,y}(x, y, -z, \psi), \tag{19}$$

$$B_z(x, y, z, -\psi) \;=\; B_z(x, y, -z, \psi). \tag{20}$$

To construct the bubble model field with the needed symmetry properties, it suffices to combine the field components (16) of the X-oriented bubbles as

$$\mathbf{b}_{\perp\, i}^{\{X\}}(\mathbf{r'}) = \mathbf{b}_i^{\{X\}}(x', y', z'^+) - \mathbf{b}_i^{\{X\}}(x', y', z'^-), \tag{21}$$
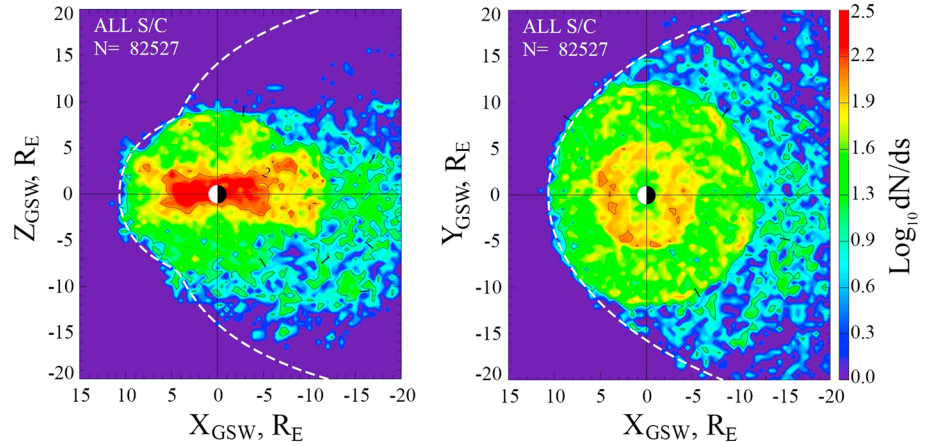
Figure 4. Distribution of spacecraft data: (left) in the noon-midnight meridian and (right) equatorial planes. The color-coded quantity is the logarithm of the column-integrated number of data records, falling into $0.5 \times 0.5\,R_E$ intervals of Geocentric Solar-Wind Magnetospheric (GSW) coordinates (with X axis-oriented antiparallel to the actual solar wind speed). Average position of the magnetopause according to Lin et al. (2010) model is shown by white-dashed line.

$$\mathbf{b}_{\parallel\,i}^{\{X\}}(\mathbf{r}') = \mathbf{b}_i^{\{X\}}(x', y', z'^+) + \mathbf{b}_i^{\{X\}}(x', y', z'^-), \tag{22}$$

and the field components (17) of the Z-oriented bubbles as

$$\mathbf{b}_{\perp\,i}^{\{Z\}}(\mathbf{r}') = \mathbf{b}_i^{\{Z\}}(x', y', z'^+) + \mathbf{b}_i^{\{Z\}}(x', y', z'^-), \tag{23}$$

$$\mathbf{b}_{\parallel\,i}^{\{Z\}}(\mathbf{r}') = \mathbf{b}_i^{\{Z\}}(x', y', z'^+) - \mathbf{b}_i^{\{Z\}}(x', y', z'^-), \tag{24}$$

where the coordinates $z'^+ = z - z_i$ and $z'^- = z + z_i$ refer to the grid nodes located symmetrically above and below the SM equatorial plane, respectively.

The final form of bubble part of the model will therefore read as an expansion over N grid nodes

$$\mathbf{B} = \cos\Psi \sum_{i=1}^{N} \left(a_{\perp\,i}^{\{X\}} \mathbf{b}_{\perp\,i}^{\{X\}} + a_{\perp\,i}^{\{Z\}} \mathbf{b}_{\perp\,i}^{\{Z\}} \right) + \sin\Psi \sum_{i=1}^{N} \left(a_{\parallel\,i}^{\{X\}} \mathbf{b}_{\parallel\,i}^{\{X\}} + a_{\parallel\,i}^{\{Z\}} \mathbf{b}_{\parallel\,i}^{\{Z\}} \right), \tag{25}$$

containing $4N$ unknown coefficients to be found from the data. In the present realization of the model, the total number of parameters is twice as high, because the coefficients $a_{\perp\,i}^{\{X\}}$, $a_{\perp\,i}^{\{Z\}}$, $a_{\parallel\,i}^{\{X\}}$, $a_{\parallel\,i}^{\{Z\}}$ are further expanded into binomials with a generic form $a + b(\sqrt{P_{dyn}/P_0} - 1)$, to take into account variations of the solar wind ram pressure P_{dyn} around its average value P_0.

The node grid in this model is based on the same Kurihara (1965) meshwork as that used in our previous works (Andreeva & Tsyganenko, 2016; Tsyganenko & Andreeva, 2016, 2017, 2018); the only difference is in the grid's spatial extent and resolution. In this study, the main goal was to represent the large-scale diamagnetic cavities in the outer cusps, which do not penetrate into the magnetosphere deeper than down to $R = 5 - 6\,R_E$. Based on this, the grid inner boundary was placed at $R = 5\,R_E$, and the angular resolution of the grid was set at 10°. Combined with restrictions on the grid tailward extent $X_{SM} \geq -5\,R_E$, this resulted in 959 nodes in the northern hemisphere. Owing to the assumed symmetry relations implied by (18)–(25), there was no need to duplicate the grid nodes into the southern hemisphere.

3. Data

As in all our recent works, the data used in the present study were selected from a periodically updated "grand" data pool of 5-min average magnetospheric magnetic field vectors, provided by magnetometer experiments onboard Geotail, Polar, Cluster, Themis, and Van Allen missions. Each data record is tagged with concurrent interplanetary parameters and ground activity indices from OMNI data resource. The entire database covers now more than two decades from 1995 through 2016 and includes a total of 4,787,162 five-min average records. A synopsis of the contributing spacecraft was presented earlier in Tsyganenko and Andreeva (2015,
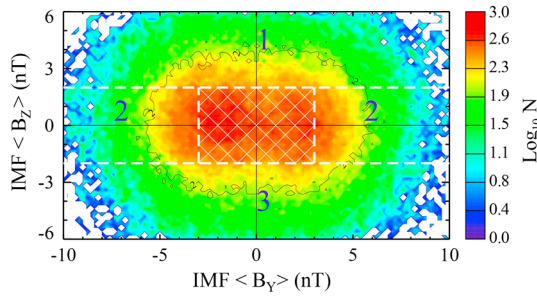
Figure 5. Distribution of the data on the IMF $\langle B_y \rangle - \langle B_z \rangle$ plane. The color-coded quantity is the logarithm of the number of data records, falling into 0.2×0.2 nT intervals of the corresponding IMF components. The data subset numbers (see text) are shown in each of the three B_y/B_z areas. White-dashed lines mark the subset boundaries, and the cross-hatched rectangle delineates the region of weak B_y and B_z, not included in the subset #2. IMF = interplanetary magnetic field.

Section 2), a detailed account of the last available version of the grand data pool was given in Tsyganenko and Andreeva (2017, Section 3), and a systematic step-by-step description of all procedures involved in the data preparation can be found in our most recent publication (Andreeva & Tsyganenko, 2018, Section 4). These papers give a fairly complete overview of all data related issues, for which reason we do not to reiterate them again and refer the reader to the above cited works for more details.

Following the above outlined hybrid strategy of the model construction, the first step was to calculate parameters of the large-scale background model, representing the average, that is, quiet and weakly disturbed configurations, based on the original *TA15* elements, such as the magnetopause, TC, SRC, PRC, and unmodified FAC modules. To that end, a subset was created from the entire grand data pool, including the magnetospheric field data taken sunward from $X_{GSM} = -20\,R_E$. In the interplanetary parametric space, the data were restricted to the following intervals of the solar wind ram pressure, speed, and IMF: $1.5 \leq P_{dyn} \leq 2.5$ nPa, $350 \leq V \leq 500$ km/s, $|B_x| \leq 7$ nT, $4 \leq |B_y| \leq 10$ nT, and $|B_z| \leq 2$ nT, respectively. Also, data records corresponding to strongly disturbed intervals were eliminated by placing limits on the Sym-H index: $-20 \leq Sym-H \leq +10$ nT. Since one of the goals of this study was to model the IMF B_y effects in the high-latitude dayside FAC structure, we intentionally excluded from the data subset all records with low absolute values of IMF B_y, which not only helped to highlight the dawn-dusk asymmetries but also reduced the size of the subsets and, hence, the computation times.

The total number of data records satisfying the above restrictions was found equal to 82,527. Figure 4 illustrates the data distribution in the noon-midnight meridional ($Y = 0$) and equatorial ($Z = 0$) projections. The color-coded quantity is the logarithm of the total number dN/dS of data points falling within $0.5 \times 0.5\,R_E$ columns of $\Delta X \times \Delta Z$ and $\Delta X \times \Delta Y$ (to avoid singular log values, we set $dN/dS = 1$ in the data gap areas). As can be seen from the plots, the data appear to be most dense in the near-equatorial region within the geocentric distance range $r \leq 5\,R_E$, where Van Allen and THEMIS missions were the principal data contributors. The high-latitude areas, including the polar cusps, are covered mainly by Polar and Cluster observations, and the data are significantly sparser there, though the difference is partly due to the columnar summation effect.

As already noted in the beginning of section 2, the cusp diamagnetism and the IMF B_y effects in the dayside R1 FAC structure were introduced in the second phase of the model calculations. The geometrical characteristics of the TC, its sensitivity to the solar wind pressure variations, and the radial decrease rate of the nightside field were treated at that step as already known fixed parameters. This made it possible to partially decouple the tail module from the fitting procedure, decrease the number of nonlinear unknowns, and shift the focus of the modeling to the dayside sector. Accordingly, three new data subsets were created, in all of which the data were limited from the nightside by $X_{GSW} \geq -5\,R_E$, and the records were sorted into three regions on the IMF $B_y - B_z$ plane: (#1) $|B_y| \leq 10$ and $2 \leq B_z \leq 6$, (#2) $3 \leq |B_y| \leq 10$ and $|B_z| \leq 2$, and (#3) $|B_y| \leq 10$ and $-6 \leq B_z \leq -2$, as illustrated in Figure 5. The purpose of excluding the central region with weak IMF B_y and B_z (and with the largest data density) was twofold: (1) to reduce the size of data sets to a manageable level and (2), most importantly, to enhance the relative contribution of data with large azimuthal IMF, in order to more distinctly reveal its effect in the dayside splitting of the model R1 FACs. The same limits $|B_x| \leq 10$ and

Table 1
Statistics of the Sequential Fitting Results for Three Data Subsets

Set #	N	IMF $\langle B_z \rangle$	$\langle B_{ext} \rangle$ (nT)	$\langle \Delta B_1 \rangle$ (nT)	$\langle \Delta B_2 \rangle$ (nT)	$\Delta B_1 / \langle B_{ext} \rangle$ (%)	$\Delta B_2 / \langle B_{ext} \rangle$ (%)
1	97,109	[+2.0, +6.0]	22.33	9.53	7.94	43	36
2	128,743	[−2.0, +2.0]	26.03	11.15	9.59	43	37
3	81,172	[−6.0, −2.0]	34.53	13.46	11.74	39	34

Note. The entries include the number N of data records, IMF $\langle B_z \rangle$ range, r.m.s. external $\langle B_{ext} \rangle$, r.m.s. residuals before (ΔB_1) and after (ΔB_2) the next-order fitting round with bubble source expansions, and their percentages relative to $\langle B_{ext} \rangle$. IMF = interplanetary magnetic field.
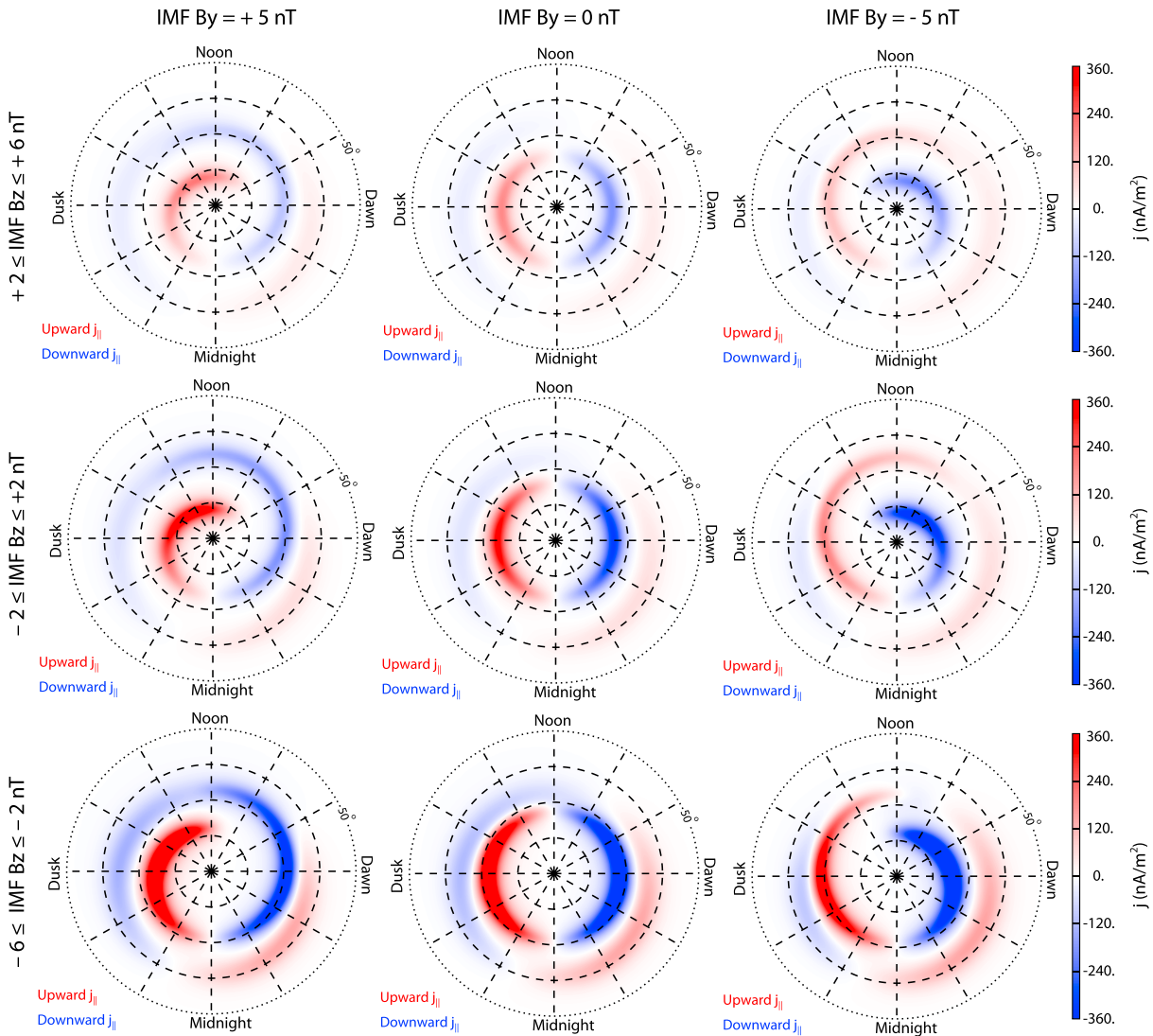
Figure 6. Polar diagrams of the model field-aligned current distribution at the ionospheric altitude, for three values of IMF $B_y = 5$ nT (left column), $B_y = 0$ (center column), and $B_y = -5$ nT (right column) and three intervals of IMF B_z: $2 \leq B_z \leq 6$ nT (top row), $|B_z| \leq 2$ nT (middle row), and $-6 \leq B_z \leq -2$ nT (bottom row). Red and blue colors indicate the upward and downward field-aligned current direction. IMF = interplanetary magnetic field.

$1.5 \leq P_{dyn} \leq 3.0$ nPa were imposed on the solar wind pressure and IMF in all three subsets, which resulted in the corresponding total numbers of data records equal to 97,109, 128,743, and 81,172. The average magnitude values of the observed external field (i.e., with the International Geomagnetic Reference Field contribution subtracted) for the three subsets were equal to $\langle B_{ext} \rangle = 22.33$, 26.03, and 34.53 nT, respectively (see section 4 and Table 1 below for more details).

4. Results

The principal objects of the present study were (1) the R1 FACs and IMF B_y effects in their dayside structure and (2) the polar CD depressions, their spatial extent, intensity, and north-south asymmetry due to the geodipole tilt. As already noted above, the corresponding sources were included into the field model in a sequential fashion. That is, in the first round of iterations, only the background base model was fitted to the extended data set, covering both the dayside and the tail region down to $X = -20\,R_E$. After that, the obtained geometrical parameters of the nightside sources were fixed, and the new modules entered into the optimization process, based on three new data subsets covering mostly the dayside sector sunward from $X = -5\,R_E$. The model fitting was performed as an iterative procedure, combining a Nelder-Mead downhill search of nonlinear parameters with an Singular
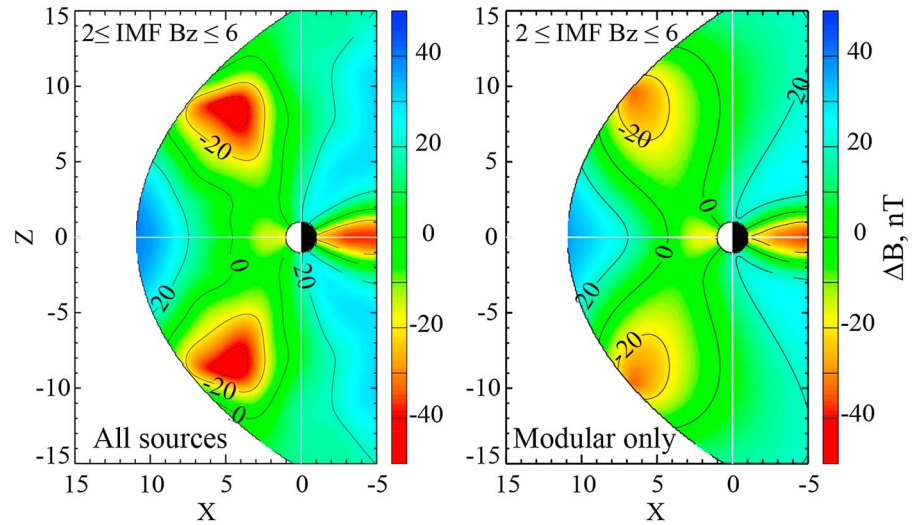
Figure 7. Meridional diagrams of the *scalar anomaly* $\Delta B = |\mathbf{B}_{total}| - |\mathbf{B}_{dipole}|$, a measure of the magnetospheric field depression (red/yellow) and compression (blue). The diagrams correspond to the model variant based on the subset #1 with positive IMF B_z. Left and right panels correspond, respectively, to the full hybrid model and to only its modular component. Note much deeper cusp depressions in the full model. IMF = interplanetary magnetic field.

Value Decomposition (SVD)-based evaluation of linear parameters (coefficients) at each simplex step (Press et al., 1992, Chapters 10.4 and 2.6). In total, the modular part of the model (i.e., without the bubble-based CD sources) included 11 coefficients quantifying the magnitudes of the individual modules and their modulation by the dipole tilt angle and 20 nonlinear parameters, of which six, five, and nine referred to the TC, SRC/PRC, and R1 FAC systems, respectively.

4.1. Field-Aligned Currents

The parameters $\Delta\phi$ and $\Delta\theta_1$, specifying, respectively, the azimuthal overlap and colatitude separation between the downward and upward curtains of the R1 FACs near noon (see Figure 2), are represented in the model as linear functions of IMF B_y

$$\Delta\phi = \Delta\phi_0 \left| B_y^{\{IMF\}}/5 \right| \quad \text{and} \quad \Delta\theta_1 = \Delta\theta_{1,0} \left(B_y^{\{IMF\}}/5 \right), \tag{26}$$

such that larger values of $\left| B_y^{\{IMF\}} \right|$ result in a larger longitudinal overlap and wider north-south separation between the duskside and dawnside FAC segments. In the case $B_y^{\{IMF\}} = 0$, the splitting vanishes, and the FAC oval becomes closed and symmetric with respect to the noon meridian. The IMF B_y in (26) is normalized by its average magnitude 5 nT, and the coefficients $\Delta\phi_0$ and $\Delta\theta_{1,0}$ are treated as free nonlinear parameters of the model to be found from data.

As expected, the noon colatitude θ_0 of the R1 FAC zone entering in (2)–(6) was found to clearly depend on the IMF B_z, varying from 14.5° for the subset #1 ($2 \leq B_z^{\{IMF\}} \leq 6$; see Figure 5), to 15.9° for subset #2 ($|B_z^{\{IMF\}}| \leq 2$), and to 17.5° for the subset #3 ($-6 \leq B_z^{\{IMF\}} \leq -2$), due to the overall expansion of the R1 FAC oval caused by enhanced dayside reconnection. The corresponding values of its noon-midnight increment $\Delta\theta_0$ were found to be rather small, not exceeding 1.7° of latitude.

The best-fit values of the proportionality coefficients $\Delta\phi_0$ and $\Delta\theta_{1,0}$ in (26) in all trial runs invariably converged to positive values, consistent with the expected deformation pattern based on both AMPERE and MHD simulation results (e.g., Korth et al., 2010, 2011). More quantitatively, for the same subsets #1, 2, and 3, the following values (expressed in degrees) were obtained, respectively: $\Delta\phi_0 = 63°$, 50°, and 12° and $\Delta\theta_1 = 6.5°$, 7.7°, and 5.4°. The resulting low-altitude distributions of the FAC density in the northern hemisphere are shown in Figure 6. The top, middle, and bottom rows correspond to the model variants derived from the subsets #1, 2, and 3, composed of the data for IMF $B_z \geq 2$, $|B_z| \leq 2$, and $B_z \leq -2$, respectively. The left, center, and right columns correspond to IMF $B_y = +5$, $B_y = 0$, and $B_y = -5$ nT.

As expected, the equatorward expansion of both the R1 and R2 FAC zones is accompanied with a dramatic increase of the overall strength of the FACs, as the IMF B_z changes from northward to southward: the magnitude coefficients for the R1 FAC module, obtained from the subsets #1, 2, and 3, were found equal to 0.42, 0.80,
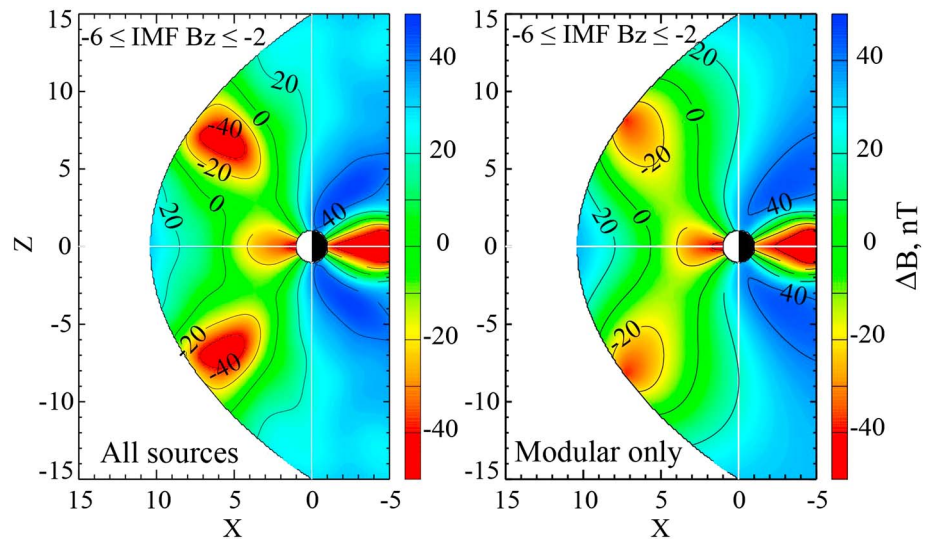
Figure 8. Same as in Figure 7 but based on the negative IMF B_z data subset #3. IMF = interplanetary magnetic field.

and 1.54, respectively, roughly corresponding to the values in mega-Amperes of total inflowing/outflowing current per hemisphere. The spiral FAC patterns, as well as the poleward shrinking of the opposite FAC branches in the case of IMF $B_y \neq 0$, agree reasonably well with those obtained from AMPERE data and global MHD simulations (e.g., Korth et al., 2010, 2011). Note that the FAC configurations in the left and right columns are not completely mirror symmetric, which is due to the fact that, unlike the R1 FACs, the PRC and associated R2 FACs are virtually insensitive to the IMF B_y, such that their azimuthal rotation remains duskward in all three cases.

It should be noted that the latitude gaps between the near-noon dawn and dusk parts of the R1 FAC oval are significantly wider than those obtained from low-altitude AMPERE data and based on MHD simulations (Korth et al., 2011, Figure 3). Also, in the upper row of plots in our Figure 6 for IMF $B_z > 0$, the FAC patterns retain the same oval-shaped geometry as in the center and bottom diagrams, while the low-altitude data reveal a dramatic shrinking of the currents within a narrow area, especially pronounced in the case of IMF $B_y \sim 0$. The most likely cause of the discrepancy is the lack of the model's flexibility, both in regard to the azimuthal variation of FAC density and to their closure in the distant magnetosphere, discussed above in the end of section 2.1.2.
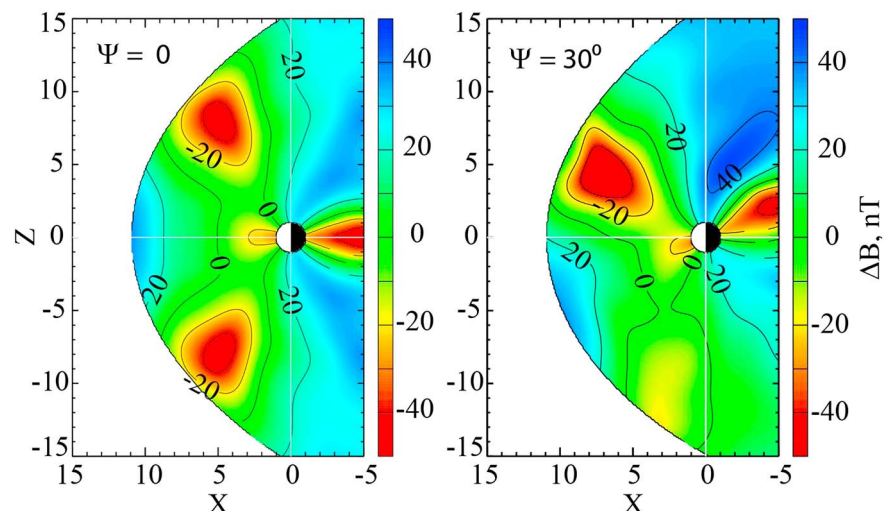

Figure 9. Illustrating the effect of the dipole tilt angle in the North-South asymmetry of the polar cusp depressions.
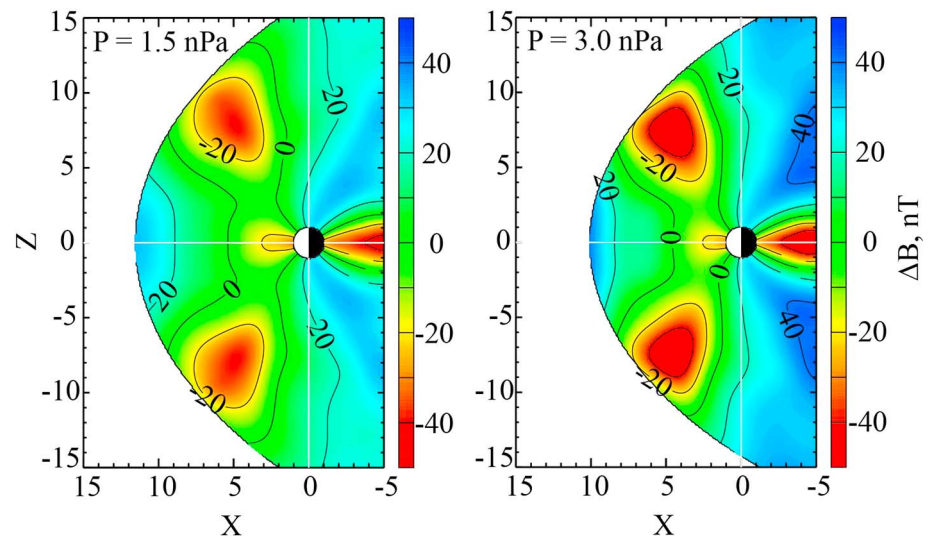
Figure 10. Illustrating the effect of the solar wind pressure on the dayside distribution of the magnetospheric field compression/depression.

4.2. Cusp Diamagnetic Sources

The cusp depression module was represented by the expansion (25) over the bubble basis functions, which included in total 7,672 unknown coefficients, obtained by minimizing the r.m.s. residual difference between the observed set of magnetic field vectors and that produced by the previously derived modular component of the model. The calculation algorithm included an Message Passing Interface (MPI)-based program that generated a matrix and right-hand side vector of a normal equation system and an SVD inversion code used to derive the final solution. The relative role of the cusp currents can be appreciated by comparing the residual r.m.s. values of the model field deviation from data, calculated before and after the inclusion/fitting of the cusp bubble component. The corresponding results are shown in Table 1, in which $\langle B_{ext} \rangle$, $\langle \Delta B_1 \rangle$, and $\langle \Delta B_2 \rangle$ are, respectively, the r.m.s. values of the external field and the fitting residuals without and with the bubble expansions.

Comparing the percentages in the last two columns, it can be seen that the full hybrid model significantly outperforms its modular component in all three cases. Specific details behind these numbers are visualized in Figure 7 as two meridional distributions of the scalar difference $\Delta B = |\mathbf{B}_{total}| - |\mathbf{B}_{dipole}|$ between the magnitudes of the total model field $|\mathbf{B}_{total}| = |\mathbf{B}_{dipole} + \mathbf{B}_{ext}|$ and its dipolar part $|\mathbf{B}_{dipole}|$. Regions of depressed and compressed magnetic field are clearly visible as red and blue areas, respectively.

Model diagrams in this figure were generated from the model variant based on data subset #1, corresponding to positive IMF B_z polarity and illustrate the difference between the ΔB distributions for the same IMF interval, but obtained from the full hybrid model (left panel) and from only its modular component (right panel).

Figure 8 shows a similar pair of plots, but corresponding to the model variant based on the subset #3 for negative IMF B_z.

As can be seen from comparing Figures 7 and 8, the most conspicuous differences between the cases of southward and northward IMF B_z are the following. (1) The subsolar field compression is much weaker in the case of negative IMF B_z, which is especially pronounced in the full hybrid variant of the model (left plots). The weakening of the subsolar field is due to the combined effect of the IMF reconnection/penetration, accompanied by a dramatic enhancement of R1 FACs on the dayside, as has been widely discussed in the literature since long ago (e.g., Tsyganenko & Sibeck, 1994, and references therein). (2) The polar cusp depressions are more confined in space, move closer to Earth, and shift to lower latitudes in the case of southward IMF. Again, although these effects can be discerned even in the modular component of the model (right plots), they are much more pronounced in the full version. (3) The low-latitude field depression and the tail lobe compression are much stronger in the case of southward IMF, which is a well-known and naturally expected feature of the disturbed magnetosphere.

5. Discussion and Conclusions

While the IMF B_z effects are analyzed in this study by binning the data into subsets, the solar wind pressure P_{dyn} and the dipole tilt angle Ψ analytically enter in the coefficients of the bubble field expansion (25), which allows to more accurately evaluate their impact on the polar cusp structure.

Figure 9 compares the meridional ΔB plots for $\Psi = 0°$ (left) and $\Psi = 30°$ (right), calculated for the average solar wind pressure $P_{dyn} = 2$ nPa using the hybrid model version based on the intermediate IMF B_z data subset #2 ($|B_z| \leq 2$ nT). In the symmetric case with $\Psi = 0$, the cusp depressions peak at the radial distance $R \approx 9.4\,R_E$ ($X = 4.9$, $Z = \pm 8.0$), where $\Delta B = -48$ nT. In the tilted configuration, by contrast, one observes a dramatic asymmetry, with the northern cusp depression peaking at $R \approx 8.7$ ($X = 7.4$, $Z = 4.6$) where $\Delta B = -77.3$ nT, while the southern depression is much weaker, with $\Delta B = -19.8$ nT at $R \approx 13\,R_E$ ($X = 3.1$, $Z = -12.7$).

Figure 10 illustrates the effect of the solar wind pressure. The left and right diagrams correspond, respectively, to $P_{dyn} = 1.5$ and 3.0 nPa. Although both the model magnetopause and the depressed field areas move closer to Earth in the latter case, the depression peaks remain at virtually the same location ($X = 4.8$, $Z = \pm 7.8$). Nevertheless, the twice larger solar wind pressure $P_{dyn} = 3.0$ results in a much deeper depression peak, $\Delta B = -62.6$ nT, as compared to $\Delta B = -39.1$ nT in the case of $P_{dyn} = 1.5$.

As a general comment with regard to the plots in Figures 7–10, the model field depressions are inevitably broader in latitude than in actuality, because of the very dynamic behavior of the cusps, their high sensitivity, and quick response to the interplanetary conditions, on the one hand, as well as due to our rather primitive criterion of sorting the data into the subsets, on the other. This can be ascertained, for example, by comparing the left plot in Figure 8 with a similar plot in the left and middle panels of Figure 2 of Tsyganenko and Andreeva (2018), showing an "instantaneous" polar cusp depression obtained in an MHD simulation with nearly the same interplanetary input. The simulated cusps protrude inward to nearly the same geocentric distance but are somewhat narrower in latitude. This points out the need to develop more accurate parameterization techniques in the future modeling projects.

Another noteworthy aspect concerns the fringe properties of the bubble source representation. In this model, the innermost layer of the bubble grid was placed at $r = 5\,R_E$, under assumption (supported by the above mentioned MHD simulations) that the cusp depressions do not approach significantly closer to Earth. However, there is no a priori guarantee of a regular behavior of the bubble field expansion outside the grid. A convincing and encouraging evidence in this respect is the lack of any irregular structures in the ΔB contours in the innermost magnetospheric region at $r \leq 5\,R_E$. This issue can have important implications with regard to feasibility of using bubble and/or radial basis function sources in the future empirical models, based on sets of limited and unevenly spaced simultaneous data from a constellation of satellites.

To summarize, in this work we developed an advanced model of the R1 FAC system, taking into account for the first time the IMF-related splitting and overlapping of the near-noon FAC curtains, manifested in space magnetometer data in the form of highly correlated interplanetary and magnetospheric B_y. The splitting parameters of the new model FAC system have been represented as functions of the concurrent IMF B_y and fitted to three subsets of data taken in the inner and distant magnetosphere, corresponding to three intervals of the IMF B_z. The obtained low-altitude FAC patterns were found to be in general agreement with existing observations and MHD simulations. Another important factor in the dayside magnetic field structure, largely ignored in previous data-based models, is the diamagnetic depression in the distant polar cusps. In this study, we employed a newly developed bubble representation of the magnetic field to describe the depressions in a framework of a hybrid approach, in which the modular component serves as a first-approximation model, while the bubble expansion plays the role of a higher-order correction. The model cusp structure has been studied with respect to its dependence on the solar wind pressure, IMF B_z, and the dipole tilt angle. The primary factors affecting the magnitude of the cusp depression are the solar wind pressure and the dipole tilt angle, while the IMF B_z orientation was found to be of secondary importance in that regard.

References

Andreeva, V. A., & Tsyganenko, N. A. (2016). Reconstructing the magnetosphere from data using radial basis functions. *Journal of Geophysical Research: Space Physics*, *121*, 2249–2263. https://doi.org/10.1002/2015JA022242

Andreeva, V. A., & Tsyganenko, N. A. (2018). Empirical modeling of the quiet and storm time geosynchronous magnetic field. *Space Weather*, *16*, 16–36. https://doi.org/10.1002/2017SW001684

Carter, J. A., Milan, S. E., Coxon, J. C., Walach, M.-T., & Anderson, B. J. (2016). Average field-aligned current configuration parameterized by solar wind conditions. *Journal of Geophysical Research: Space Physics*, *121*, 1294–1307. https://doi.org/10.1002/2015JA021567

Erlandson, R. E., Zanetti, L. J., Potemra, T. A., & Bythrow, P. F. (1988). IMF B_y dependence of region 1 Birkeland currents near noon. *Journal of Geophysical Research*, *93*, 9804–9814.

Fairfield, D. H. (1991). An evaluation of the Tsyganenko magnetic field model. *Journal of Geophysical Research*, *96*, 1481–1494.

Farrell, W. M., & Van Allen, J. A. (1990). Observations of the Earth's polar cleft at large radial distances with the Hawkeye 1 magnetometer. *Journal of Geophysical Research*, *95*, 20,945–20,958.

Kaufmann, R. L., Paterson, W. R., & Frank, L. A. (2003). Birkeland currents in the plasma sheet. *Journal of Geophysical Research*, *108*(A7), 1299. https://doi.org/10.1029/2002JA009665

Korth, H., Anderson, B. J., & Waters, C. L. (2010). Statistical analysis of the dependence of large-scale Birkeland currents on solar wind parameters. *Annals of Geophysics*, *28*, 515–530.

Korth, H., Rastaetter, L., Anderson, B. J., & Ridley, A. J. (2011). Comparison of the observed dependence of large-scale Birkeland currents on solar wind parameters with that obtained from global simulations. *Annals of Geophysics*, *29*, 1809–1826.

Kurihara, Y. (1965). Numerical integration of the primitive equations on a spherical grid. *Monthly Weather Review*, *93*(7), 399–415.

Laundal, K. M., Finlay, C. C., Olsen, N., & Reistad, J. P. (2018). Solar wind and seasonal influence on ionospheric currents from Swarm and CHAMP measurements. *Journal of Geophysical Research: Space Physics*, *123*, 4402–4429. https://doi.org/10.1029/2018JA025387

Lin, R. L., Zhang, X. X., Liu, S. Q., Wang, Y. L., & Gong, J. C. (2010). A three-dimensional asymmetric magnetopause model. *Journal of Geophysical Research*, *115*, A04207. https://doi.org/10.1029/2009JA014235

McDiarmid, I. B., Burrows, J. R., & Wilson, M. D. (1979). Large-scale magnetic field perturbations and particle measurements at 1400 km on the dayside. *Journal of Geophysical Research*, *84*(A4), 1431–1441.

Mead, G. D., & Fairfield, D. H. (1975). A quantitative magnetospheric model derived from spacecraft magnetometer data. *Journal of Geophysical Research*, *80*, 523–534.

Newell, P. T., & Meng, C.-I. (1989). Dipole tilt angle effects on the latitude of the cusp and cleft/low-Latitude boundary layer. *Journal of Geophysical Research*, *94*(A6), 6949–6953.

Press, W. H., Teukolsky, S. A., Vetterling, W. T., & Flannery, B. P. (1992). *Numerical Recipes* (2nd ed.). New York: Cambridge University Press.

Reiff, P. H., & Burch, J. L. (1985). IMF B_y-dependent plasma flow and Birkeland currents in the dayside magnetosphere 2. A global model for northward and southward IMF. *Journal of Geophysical Research*, *90*(A2), 1595–1609.

Sergeev, V. A., Tsyganenko, N. A., Smirnov, M. V., Nikolaev, A. V., Singer, H. J., & Baumjohann, W. (2011). Magnetic effects of the substorm current wedge in a "spread-out wire" model and their comparison with ground, geosynchronous, and tail lobe data. *Journal of Geophysical Research*, *116*, A07218. https://doi.org/10.1029/2011JA016471

Sotirelis, T., Tsyganenko, N. A., & Stern, D. P. (1994). Method for confining the magnetic field of the cross-tail current inside the magnetopause. *Journal of Geophysical Research*, *99*, 19,393–19,402.

Tenfjord, P., Ostgaard, N., Snekvik, K., Laundal, K. M., Reistad, J. P., Haaland, S., & Milan, S. E. (2015). How the IMF B_y induces a B_y component in the closed magnetosphere and how it leads to asymmetric currents and convection patterns in the two hemispheres. *Journal of Geophysical Research: Space Physics*, *120*, 9368–9384. https://doi.org/10.1002/2015JA021579

Tsyganenko, N. A. (1990). Quantitative models of the magnetospheric magnetic field: Methods and results. *Space Science Reviews*, *54*, 75–186.

Tsyganenko, N. A. (2002). A model of the near magnetosphere with a dawn-dusk asymmetry: 1. Mathematical structure. *Journal of Geophysical Research*, *107*(A8), 1179. https://doi.org/10.1029/2001JA000219

Tsyganenko, N. A. (2009). Magnetic field and electric currents in the vicinity of polar cusps as inferred from Polar and Cluster data. *Annals of Geophysics*, *27*, 1573–1582. https://doi.org/10.5194/angeo-27-1573-2009

Tsyganenko, N. A. (2013). Data-based modelling of the Earths dynamic magnetosphere: A review. *Annals of Geophysics*, *31*, 1745–1772. https://doi.org/10.5194/angeo-31-1745-2013

Tsyganenko, N. A. (2014). Data-based modeling of the geomagnetosphere with an IMF-dependent magnetopause. *Journal of Geophysical Research: Space Physics*, *119*, 335–354. https://doi.org/10.1002/2013JA019346

Tsyganenko, N. A., & Andreeva, V. A. (2015). A forecasting model of the magnetosphere driven by an optimal solar wind coupling function. *Journal of Geophysical Research: Space Physics*, *120*, 8401–8425. https://doi.org/10.1002/2015JA021641

Tsyganenko, N. A., & Andreeva, V. A. (2016). An empirical RBF model of the magnetosphere parameterized by interplanetary and ground-based drivers. *Journal of Geophysical Research: Space Physics*, *121*, 10,786–10,802. https://doi.org/10.1002/2016JA023217

Tsyganenko, N. A., & Andreeva, V. A. (2017). A hybrid approach to empirical magnetosphere modeling. *Journal of Geophysical Research: Space Physics*, *122*, 8198–8213. https://doi.org/10.1002/2017JA024359

Tsyganenko, N. A., & Andreeva, V. A. (2018). Building the magnetosphere from magnetic bubbles. *Geophysical Research Letters*, *45*, 6382–6389. https://doi.org/10.1029/2018GL078714

Tsyganenko, N. A., & Russell, C. T. (1999). Magnetic signatures of the distant polar cusps: Observations by Polar and quantitative modeling. *Journal of Geophysical Research*, *104*, 24,939–24,955.

Tsyganenko, N. A., & Sibeck, D. G. (1994). Concerning flux erosion from the dayside magnetosphere. *Journal of Geophysical Research*, *99*, 13,425–13,436.

Tsyganenko, N. A., & Stern, D. P. (1996). Modeling the global magnetic field of the large-scale Birkeland current systems. *Journal of Geophysical Research*, *101*, 27,187–27,198.

Tsyganenko, N. A., Stern, D. P., & Kaymaz, Z. (1993). Birkeland currents in the plasma sheet. *Journal of Geophysical Research*, *98*, 19,455–19,464.